Int. J. Electrochem. Sci., 17 **(2022)** Article Number: 221210, doi: 10.20964/2022.12.13

International Journal of ELECTROCHEMICAL SCIENCE
www.electrochemsci.org

Graphene-incorporated Dopamine-Modified Fe_2O_3 Nanorings as Anode for High-performance Lithium Battery

Guiqing Guan[1], Jiameng Jin[2], Rongxiu Ou[1], Nuolin Lin[1], Jianping Lin[1], Hong Fu[1], Wenyu Yang[1], Hai Jia[1,2,3,] and Zhiya Lin[1,3,*]*

[1] College of Mathematics and Physics, Ningde Normal University, Ningde, 352100, China.
[2] College of Physics and Energy, Fujian Normal University, Fujian Provincial Key Laboratory of Quantum Manipulation and New Energy Materials, Fuzhou, 350117, China.
[3] College of Physics and Energy, Fujian Normal University, Fujian Provincial Solar Energy Conversion and Energy Storage Engineering Technology Research Center, Fuzhou, 350117, China.
[*]E-mail: jiahaicc@126.com (Hai Jia); zhiyalin@126.com (Zhiya Lin).

Received: 27 August 2022/ *Accepted:* 24 October 2022/ *Published:* 17 November 2022

Novel facile two-dimensional graphene-incorporated composites of dopamine-modified Fe_2O_3 (Fe_2O_3@PDA@G) nanorings were rationally fabricated and designed with electrostatic interactions to provide highly specific surface areas. The contact area of the electrolyte/electrode was increased to reduce the current density per unit surface area during the electrode reaction. Compared to bare Fe_2O_3, Fe_2O_3@PDA@G exhibited higher capacities and improved rate capability in the potential range of 0.01~3.0V. The Fe_2O_3@PDA@G composites showed a specific capacity of 727.4 $mAhg^{-1}$ at 500 mAg^{-1} after 240 cycles, while bare Fe_2O_3 only delivered a discharge capacity of 97.2 $mAhg^{-1}$. In addition, Kelvin probe force microscopy (KPFM) measurements showed that Fe_2O_3@PDA@G had a lower localized work function than that of the pristine one, which enabled Fe_2O_3@PDA@G to be more suitable for lithium-ion battery applications.

Keywords: lithium battery, graphene, Fe_2O_3 nanoring, electrostatic incorporation, KPFM

1. INTRODUCTION

Due to their environmentally benign nature and the current consumption of the world's fossil-fuel reserves, lithium-based energy systems have attracted increasing attention worldwide [1-3]. Due to their high energy density, high working voltage, lack of memory effect, low cost, low pollution, small self-discharge and good safety performance, lithium-ion batteries (LIBs) are widely used in portable electronic devices, such as mobile phones and laptops. Also, for the next generation of electric vehicles and large static energy storage systems, LIBs also have wide application potentials [4-6]. Transition metal oxides (such as Fe_3O_4, Co_3O_4, SnO_2, WO_3, and MnO_2) have been explored as alternative materials

for LIBs due to their high theoretical specific capacity [8-12]. Compared to Co_3O_4, SnO_2, WO_3, and MnO_2, haematite (α-Fe_2O_3) has become one of the most attractive transition metal oxides due to its high theoretical capacity (1005 $mAhg^{-1}$), natural abundance, low cost and environmental friendliness [13,14]. Nonetheless, like other transition metal oxides, α-Fe_2O_3 inherently has poor electrical conductivity, large volume expansion and particle aggregation during Li^+ insertion and extraction processes, leading to limited rate performance and cycle life fast fading [14-16]. In recent years, to enhance the lithium storage properties of iron oxides, various iron oxide nanostructure composites, such as graphene wrapping [17-19], carbon nanofibres and carbon nanotubes (SWCNTs or MWCNTs), have been reported [15, 20-22].

Graphene, a honeycomb network of sp^2-hybridized carbon atoms with a 2D hexagonal lattice structure, has excellent electron mobility, ultrahigh surface area and mechanical properties [23,24], which will most likely make graphene an ideal conductive additive for hybrid nanostructure electrodes [25]. Recently, many researchers have achieved many successful outcomes by mixing, coating or assembling graphene with Fe_2O_3. For example, Gu *et al.* synthesized an Fe_2O_3-SnO_2/graphene composite via a one-step hydrothermal process, and the results demonstrated outstanding cycle stability [26]. Meng *et al.* reported the synthesis of a Fe_2O_3/graphene composite using a hydrothermal method, which exhibited a specific capacity of 745 $mAhg^{-1}$ after 100 cycles at a current density of 100 mAg^{-1} [27]. In this study, we designed a simple and flexible synthesis strategy for Fe_2O_3@polydopamine@graphene (Fe_2O_3@PDA@G) nanorings by electrostatic incorporation. Electrochemical evaluation indicated that Fe_2O_3@PDA@G composites exhibit a higher discharge capacity, superior stability and excellent rate performance compared the unsatisfactory electrochemistry of bare Fe_2O_3 as anode materials for LIBs. These superior Li^+ storage properties are based on the stabilized crystal structure, unexceptionable electrical conductivity and synergistic effect between Fe_2O_3 particles and graphene sheets.

2. EXPERIMATION

2.1 Synthesis of α-Fe_2O_3 nanoparticles

Haematite (α-Fe_2O_3) nanorings were fabricated by a one-pot hydrothermal method. $FeCl_3$ (519.06 mg) was dissolved in 80 mL of deionized water. Then, 3.25 mg of NaH_2PO_4 and 12.5 mg of Na_2SO_4 were added to the suspension while stirring for 2 hours. The solution was then transferred to a 100-ml Teflon-lined stainless steel autoclave and heated at 220 ℃ for 12 h. After the mixture naturally cooled to room temperature, the red precipitate was collected by centrifugation; washed with deionized water and absolute ethyl alcohol several times; and dried under vacuum at 80 ℃ overnight.

2.2 Synthesis of Fe_2O_3@PDA@G

Typically, 0.5 g Fe_2O_3 nanorings were first dispersed into 500 mL of 10×10^{-3} m tris-buffer solution (pH=8.5) by ultrasonication for 60 min. Then, 0.25 g of dopamine hydrochloride was added into the above solution and stirred continuously for 12 h. The resultant product was collected via centrifugation; washed several times with absolute ethyl alcohol and deionized water; and dried overnight at 80 °C. A total of 100 mg of as-prepared Fe_2O_3@polydopamine (Fe_2O_3@PDA) was

dispersed in 100 mL of absolute ethyl ethanol under ultrasonication for 60 min, and then, 3 mL of 3-aminopropyltriethoxysilane (APTES) was added under continuous stirring and stirred for 5 h. The sediment collected by centrifugation was washed with ethanol several times to obtain amino-silane modified Fe_2O_3@PDA nanoparticles. Then, a certain amount of 2 M graphene oxide (GO) suspension was added to the aminosilane-modified Fe_2O_3@PDA dispersion and stirred vigorously for 2 h so that Fe_2O_3@PDA particles were strongly adsorbed on the GO surface through electrostatic interactions. Then, the sediment was collected by centrifugation and washed several times with deionized water. Finally, the final product was obtained by calcination at 400℃ under argon atmosphere for 2 h. A schematic illustration of the experimental process for Fe_2O_3@PDA@G is shown in Fig. 1.

2.3 Material characterization

The X-ray diffraction (XRD) patterns of the as-prepared powders were obtained by a Rigaku Mini-Flex II (CuKα, λ = 0.15406 nm). The surface morphology and microstructures were observed by scanning electron microscopy (SEM, Hitachi SU-8010) and transmission electron microscopy (TEM, Tecnai G2 F20 S-TWIN). The nitrogen adsorption-desorption isotherms at 77 K were obtained using a surface area and pore size analyser (TriStar II 3020). The specific surface areas and pore sizes of samples were recorded using the multipoint Brunauer–Emmett–Teller (BET) model and Barrett–Joyner–Halenda (BJH) model, respectively. Thermogravimetric and differential scanning calorimetric analysis was conducted on a TG-DSC simultaneous thermal analyser (Netzsch STA449F3) up to 600 °C under air to determine the carbon content of the sample. The graphene structure of Fe_2O_3@PDA@G was analysed by Raman spectroscopy (LabRAM HR, HORIBA JobinYvon) with a 532-nm Argon ion laser from 1000 to 2000 cm^{-1}. The surface potentials and work function detection of Fe_2O_3, Fe_2O_3@PDA and Fe_2O_3@PDA@G were measured by Kelvin probe force microscopy (KPAFM) (Bruker dimension ICON, Germany). It is a non-destructive non-contact surface technique that can image the two-dimensional profile of the contact potential difference (V_{CPD}). The V_{CPD} is defined as:

$$V = \frac{\emptyset_{tip} - \emptyset_{sample}}{q}$$

Here, V_{CPD} is defined as the work function of the $\emptyset_{tip}$ and $\emptyset_{sample}$ representing the conductive tip and sample, and q is the charge. In this study, the work functions of the SFM tip ($\emptyset_{tip}$) are calibrated by a Au foil reference sample, whose work function ($\emptyset_{tip}$) is 5.31 eV.

2.4 Cell fabrication and characterization

Electrochemical measurements were performed using coin-type CR2025-type half-cells. The cells were based on the configuration of Li metal (-)|electrolyte|Fe_2O_3-based materials (+) with a liquid electrolyte. The electrolyte consisted of a mixture of 1 M $LiPF_6$ in ethylene dimethyl carbonate (DMC)-diethyl carbonate (DEC)-carbonate (EC) (1:1:1 by volume), in which a lithium metal foil was used as the counter and reference electrode. The working electrode was prepared by a slurry coating procedure. The slurry consisted of 80-wt% active materials (Fe_2O_3 or Fe_2O_3@PDA@G), 10-wt% conductive Super P, and 10-wt% carboxymethyl cellulose (CMC) binder and deionized water. Then, the samples were

spread evenly on cleaned copper foil, dried under vacuum at 120 °C for 12 hours, cut into 12.5 mm diameter electrode discs, and then weighed. The loading density of the active substance was ~1.5 mg•cm^{-2}. The half-cell was assembled in a glove box filled with argon, with the concentration of water and oxygen in the glove box kept at ≤0.1 ppm. In addition, the constant-current charging and discharging performance of the half-cell was tested by a multichannel battery test system (Wuhan, LAND, China) at different current densities, where the potential window range was 0.01-3.0 V. The EIS impedance spectroscopy of samples was obtained using an electrochemical workstation (Zahner-Zennium) with frequencies ranging from 10 mHz to -100 kHz and an AC signal amplitude of 0.005 V.

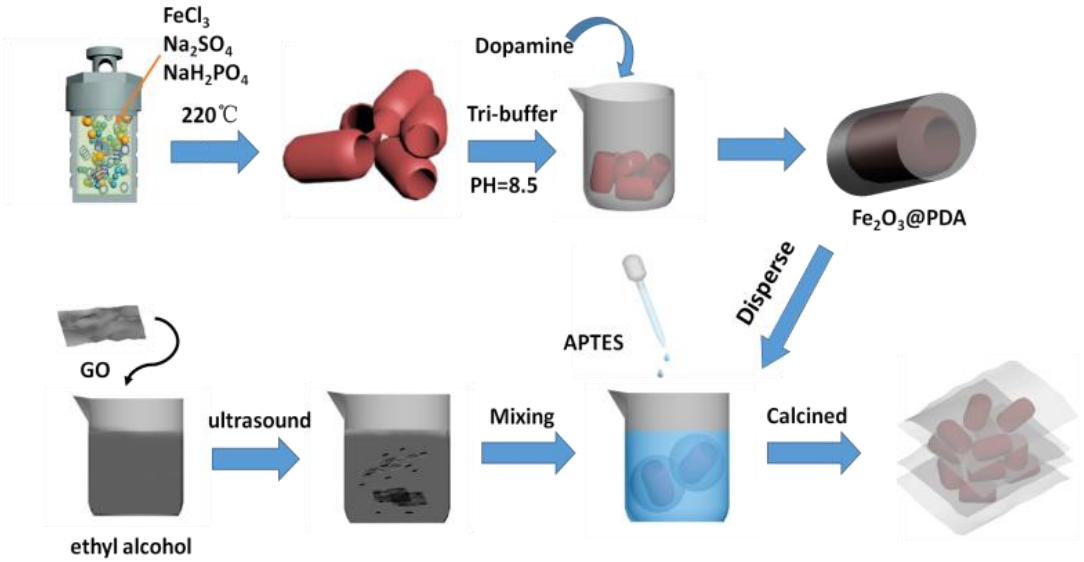

Figure 1. Schematic illustration of the preparation process of Fe_2O_3@PDA@G.

3. RESULTS AND DISCUSSION

The morphologies and microstructure of the α-Fe_2O_3 nanorings, Fe_2O_3@PDA and Fe_2O_3@PDA@G composites were examined using SEM and TEM. As shown in Fig. 2. Fig. 2(a,b) shows that the bare α-Fe_2O_3 formed with a ring-like shape with a smooth surface exhibits severe agglomeration of nanoparticles. These nanorings appear to be well distributed with 100-nm outside diameters and 50-nm inside diameters. Fig. 2(c, d) shows the surface topographies of the Fe_2O_3@PDA and Fe_2O_3@PDA@G composites, respectively. The as-synthesized Fe_2O_3@PDA and Fe_2O_3@PDA@G nanorings maintain the morphology of the Fe_2O_3 nanoring precursor with a smooth carbon layer. The thickness of the carbon layer was ~10 nm, which can be identified from the transmission electronic microscope (TEM) images (Fig. 2e and d). Concurrently, Fe_2O_3@PDA is shown to be completely encased in graphene sheets, and adjacent nanorings are connected by wrinkled graphene. This wrinkled morphology hinders restacking among these sheets, and the presence of waving markedly enhances electrochemical performance, which is manifested by improving Li-ion transportation on the entire electrode surface by shortening the Li-ion diffusion path. Nearly all Fe_2O_3 nanorings are encapsulated within the graphene sheets, forming a unique adjustable sandwich structure. In addition to facilitating

electron transfer and additional Li storage, the special sandwich structure also enables good contact between the internal active materials and the electrolyte, which effectively inhibits volume changes during Li^+ embedding and extraction [28,29].

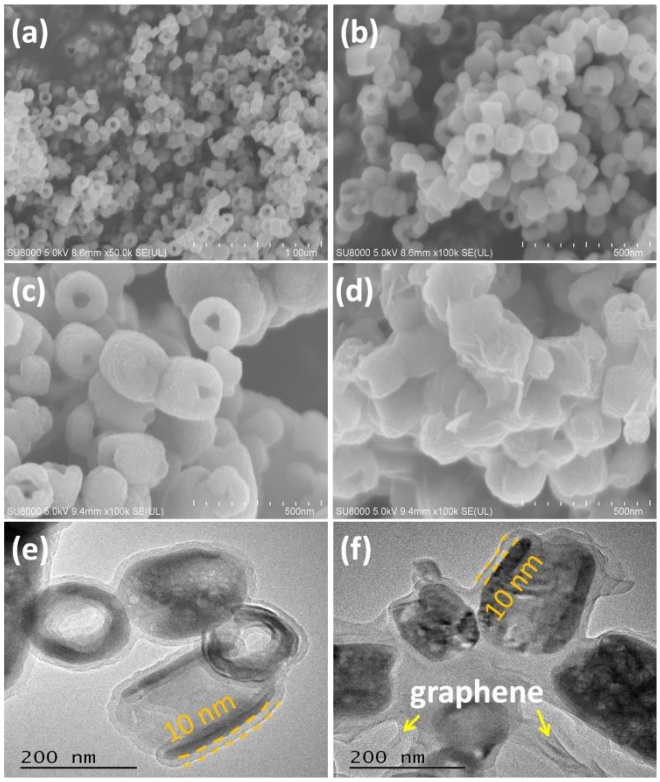

Figure 2. (a, b) SEM images of as-prepared Fe_2O_3 nanorings; (c) Fe_2O_3@PDA and (d) Fe_2O_3@PDA@G; (e) TEM images of Fe_2O_3@PDA and (f) Fe_2O_3@PDA@G.

Fig. 3(a) shows the nitrogen adsorption-desorption isotherms of Fe_2O_3, Fe_2O_3@PDA and Fe_2O_3@PDA@G. The figure shows that the isotherms of all samples conform to the typical IV isotherm characteristics of porous materials in IUPAC classification [30]. The mesoporous electrode materials were believed to be beneficial to the infiltration of the electrolyte, accelerating the diffusion of Li^+ [31]. The Brunauer–Emmett–Teller (BET) specific area of Fe_2O_3@PDA@G is 34.8 m^2/g, which is higher than that of bare Fe_2O_3 (20.8 m^2/g) and Fe_2O_3@PDA nanoparticles. A similar BJH (Barrett–Joyner–Halenda) aperture distribution is shown in Fig. 3(b). The pore-size distribution has a broad peak centred at 34 nm for samples Fe_2O_3@PDA and Fe_2O_3@PDA@G. The Fe_2O_3@PDA@G sample has another narrow peak at 4 nm with a large pore volume (0.421 cm^3/g), which can increase the contact area of the electrolyte and electrode and reduce the current density per unit surface area during the electrode reaction process. [32]. The observed result can be attributed to the uniform distribution of the layer gaps and Fe_2O_3@PDA nanoparticles on the graphene sheets [33]. To describe the composition and phase structure of Fe_2O_3, Fe_2O_3@PDA and Fe_2O_3@PDA@G, the XRD diffraction patterns are shown in Fig. 3(c). All the peaks at 2θ values of 24.4°, 33.4°, 35.9°, 39.4°, 41.0°, 43.8°, 49.4°, 54.3°, 57.7°, 62.4°, and 64.2° can be well indexed as rhombohedral α-Fe_2O_3 (JCPDS no. 33-0664), which are assigned to the (012), (104), (110), (006), (113), (202), (024), (116), (018), (214), and (300) lattice planes, respectively [27,34]. The

diffraction pattern of the Fe_2O_3@PDA@G nanocomposite agrees with the haematite phase, and a new broad peak is shown at $2\theta \approx 25^{\circ}$, which can be attributed to the (002) plane of reduced graphene [35]. The contents of graphene and dopamine in the composites were evaluated by thermogravimetric analysis (TGA), as shown in Fig. 3(d). Result shows that the thermal decomposition temperature of the as-obtained sample is approximately 350 ℃, and the weight percentage of graphene in the Fe_2O_3@PDA@G composites is calculated to be 35.75%. To investigate the structure of Fe_2O_3@PDA@G, Fig. 4 shows the Raman spectra of the as-prepared Fe_2O_3@PDA@G powders. The two broad peaks at 1344 and 1584 cm^{-1} correspond to the D-band (defect band) of the respiration mode of the A_{1g} symmetric K-point phonon and the G-band (graphite band) of the E_{2g} phonon originating from the C sp^2 atom, respectively. [36] The degree of graphitization could be evaluated by I_D/I_G, where I_D and I_G are the D and G peak intensities, respectively. The obtained ratio value (I_D/I_G=0.85) indicates a high graphitization degree of the graphene sheets in Fe_2O_3@PDA@G, which could be beneficial to the electronic conductivity improvement of the entire electrode.

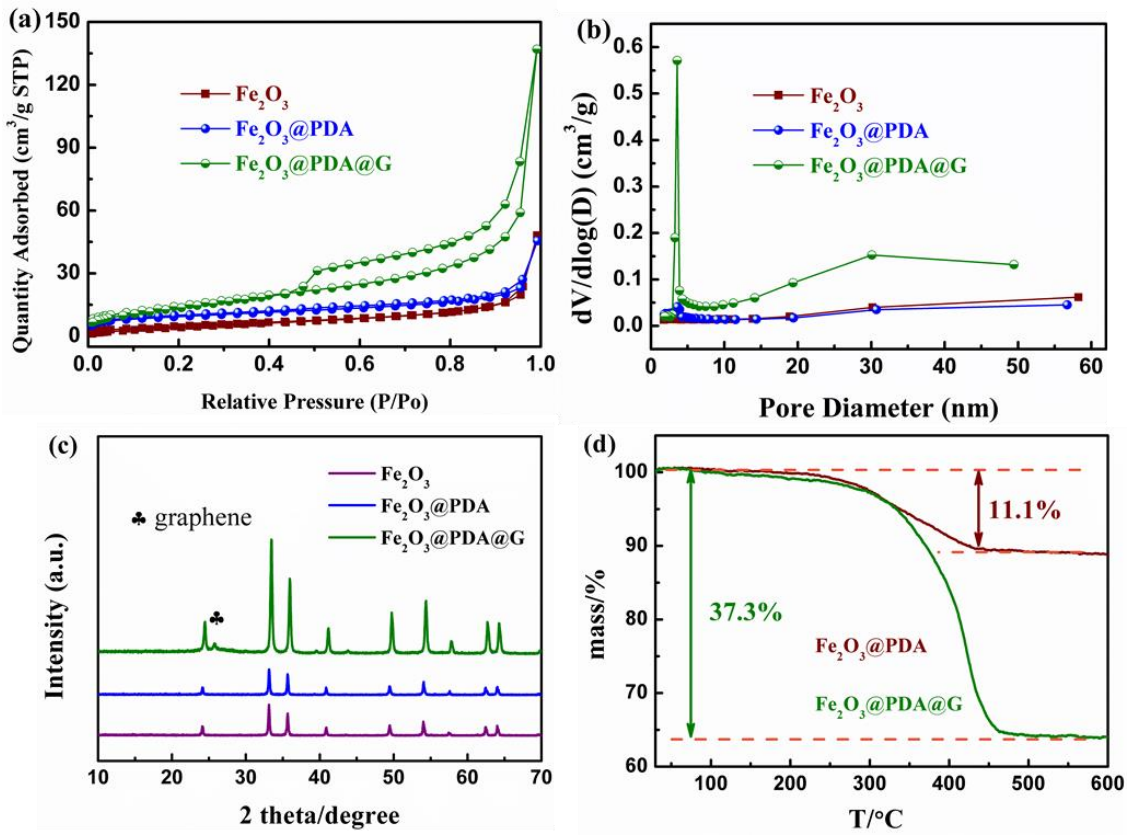

Figure 3. (a) Nitrogen adsorption-desorption isotherms of the α-Fe_2O_3 nanorings, Fe_2O_3@PDA and Fe_2O_3@PDA@G composites; (b) Barrett–Joyner–Halenda (BJH) pore size distribution of the α-Fe_2O_3 nanorings, Fe_2O_3@PDA and Fe_2O_3@PDA@G composites; (c) XRD diffraction patterns for the α-Fe_2O_3 nanorings, Fe_2O_3@PDA and Fe_2O_3@PDA@G composites; (d) thermogravimetric analysis for the α-Fe_2O_3 nanorings, Fe_2O_3@PDA and Fe_2O_3@PDA@G.

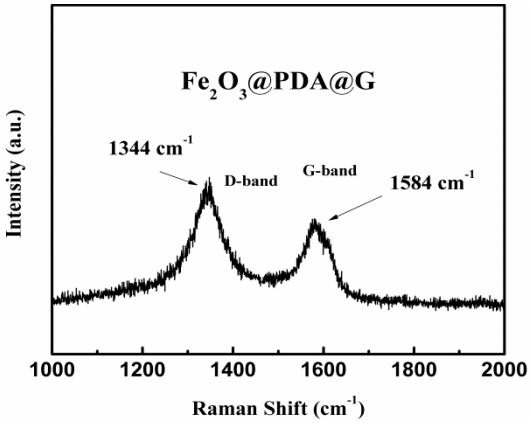

Figure 4. Raman spectra of the as-prepared Fe_2O_3@PDA@G powders.

Fig. 5(a) shows the cycling performance of Fe_2O_3, Fe_2O_3@PDA and Fe_2O_3@PDA@G at a constant cut-off potential between 0.01 V and 3.0 V vs. Li/Li^+ at a 500 mAg^{-1} current density. The cells are activated via 100 mAg^{-1} for the first cycle before cycling at 500 mAg^{-1}. The discharge capacity of the bare Fe_2O_3 decreases from 805.4 to 97.2 $mAh{\cdot}g^{-1}$ after 90 cycles, and the capacity retention ability is poor, which is only 11.51% of the initial discharge capacity. Compared with the bare Fe_2O_3 material, Fe_2O_3@PDA@G shows a higher specific capacity and stable cycling performance, which indicates that graphene involvement facilitates electron transfer and effectively reduces the degree of side reaction and thus improves the capacity cycling capacity [35]. To understand the cycling stability of Fe_2O_3@PDA@G, the structure and morphology of the aged Fe_2O_3, Fe_2O_3@PDA and Fe_2O_3@PDA@G materials after 90 cycles testing at 500 mAg^{-1} were investigated with SEM, as shown in Fig. 5(b,c,d). After discharging to 0.01 V, the coin battery was disassembled in an Argon-filled glove box; washed several times with dimethyl carbonate and absolute ethanol; and vacuum-dried overnight at 60 °C in vacuum. Fig. 5(d) shows that the aged Fe_2O_3@PDA@G composite retains its intact original nanoring structure. However, the bare Fe_2O_3 nearly collapses, indicating serious aggregation (see Fig. 5(a)). Apparently, the two-dimensional network structure of graphene contributes to the stability of composite materials during intercalation/extraction by accommodating the volume changes of the electrode during the cycling process. Electrochemical impedance spectroscopy (EIS) measurements were performed on half-cells after the 90^{th} cycle in a fully charged state for pure Fe_2O_3, Fe_2O_3@PDA and Fe_2O_3@PDA@G, as shown in Fig. 5(e). Fig. 5(e) shows that the EIS curve shows a compression semicircle in the medium frequency region and a straight slope in the low frequency region under the discharge potential of 0.1 V and within the frequency range of 100 kHz to 10 mHz, which is related to Warburg impedance and charge transfer resistance (R_{ct}) [3]. The Fe_2O_3@PDA@G electrode is shown to have a marked lower R_{ct} than that of pure Fe_2O_3. These EIS curves were fitted with the equivalent circuit shown in the illustration of Fig. 5(e), where R_{ct} and R_s are the charge transfer resistance and the solution resistance, respectively. The constant phase element (CPE) is used to represent the double-layer capacitance and passivation-film capacitance, where Z_w is the Warburg impedance [14]. The fitted results also suggest that the charge transfer resistance of Fe_2O_3@PDA@G (R_{ct}=30.31 Ω) is smaller than that of Fe_2O_3 (R_{ct}=285.6 Ω). The presence of highly conductive graphene in the composite is beneficial to reduce the total resistance and

thus effectively reduce the degree of side reactions of the electrode [35], thus enhancing the cycle stability.

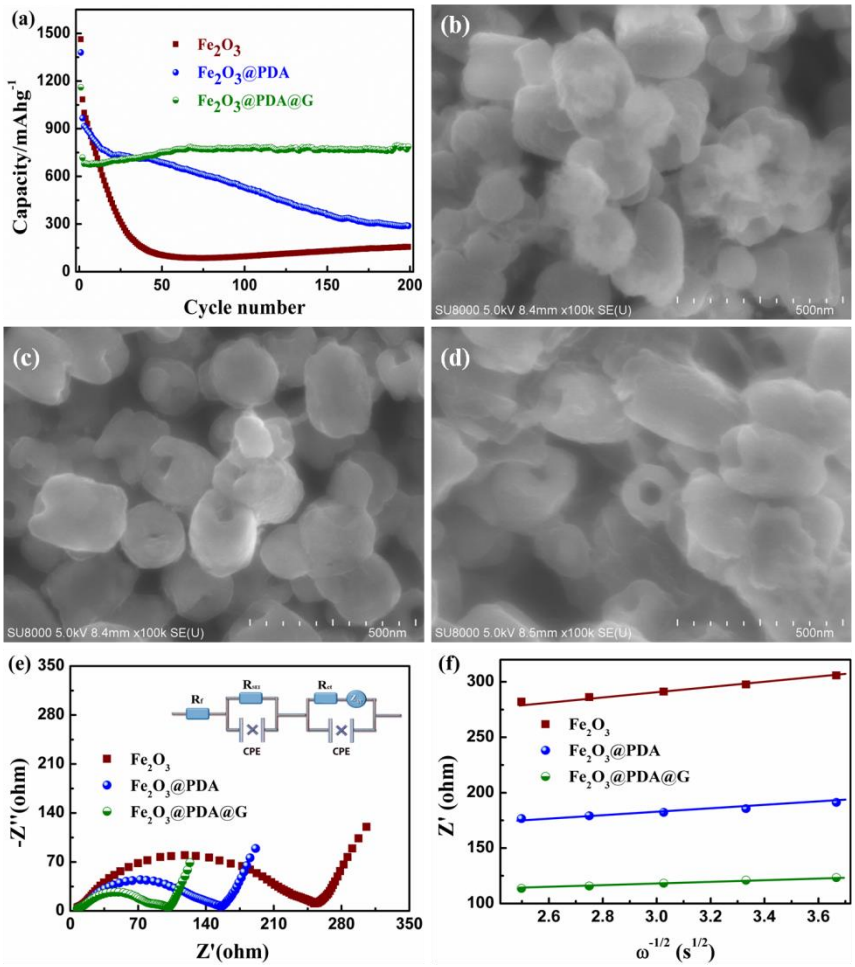

Figure 5. (a) Cycling performance of Fe_2O_3, Fe_2O_3@PDA and Fe_2O_3@PDA@G at a constant cut-off potential between 0.01 V and 3.0 V vs. Li/Li^+ at 500 mAg^{-1} current density; morphology of the aged (b) Fe_2O_3, (c) Fe_2O_3@PDA and (d) Fe_2O_3@PDA@G materials after 90 cycles testing at 500 mAg^{-1}; (e) Nyquist plots of the half-cells with pure Fe_2O_3, Fe_2O_3@PDA and Fe_2O_3@PDA@G anodes at a discharge potential of 0.1 V; (f) Relationship between Z' and $\omega^{-1/2}$ at a low frequency under ambient conditions for pure Fe_2O_3, Fe_2O_3@PDA and Fe_2O_3@PDA@G. Fe_2O_3@PDA@G has the highest Li diffusion coefficient, meaning that Fe_2O_3@PDA@G possesses better reaction kinetics than Fe_2O_3. This result also signifies that the synergistic modification of polydopamine and graphene contributes markedly to the improvement of the lithium ion transfer kinetics within the electrode, which is in accordance with the better cycle performances.

The kinetics of Li^+ removal and charge transfer on electrode/electrolyte interfaces strongly affect the electrochemical performance of the as-synthesized electrode [4]. Fig. 5(f) shows the relationship between Z' and $\omega^{-1/2}$ for pure Fe_2O_3, Fe_2O_3@PDA and Fe_2O_3@PDA@G. In this study, the lithium ion diffusion coefficient (D_{Li}) can be calculated from the following theoretical Equations (1) and (2):

$$Z' = R_{ct} + R_s + \sigma\omega^{-1/2}, \quad (1)$$

$$D_{Li} = \frac{R^2T^2}{2A^2n^4F^4C_{Li}^2\sigma^2}, \quad (2)$$

where Z' is the total resistance of charge transfer resistance (R_{ct}) and solution resistance (R_s); σ, ω, R, T and n are the Warburg factor, angular frequency, gas constant, absolute temperature and number of electrons per molecule in the redox process, respectively; and A, F, and C_{Li} are the electrode surface area, Faraday constant and lithium ion concentration, respectively. The corresponding lithium ion diffusion coefficients D_{Li} for pure Fe_2O_3, Fe_2O_3@PDA and Fe_2O_3@PDA@G are calculated as 2.97×10^{-13}, 8.19×10^{-13} and 1.69×10^{-12}, respectively. According to the above result, Fe_2O_3@PDA@G has the highest Li diffusion coefficient of the tested materials; thus, Fe_2O_3@PDA@G exhibits better reaction kinetics than Fe_2O_3. This result also indicates that the synergistic modification of polydopamine and graphene strongly contributes to the improvement of the lithium ion transfer kinetics within the electrode, which produces better cycle performances. To investigate the mechanism of the electrochemical reactions, the bare Fe_2O_3, Fe_2O_3@PDA and Fe_2O_3@PDA@G nanomaterials were studied with cyclic voltammetry (CV) measurements. Fig. 6 shows the cyclic voltammetry curves of the Fe_2O_3, Fe_2O_3@PDA and Fe_2O_3@PDA@G electrodes in the first cycle in the voltage range of 0.01~3 V at a scan rate of 0.1 mV/s. In the first cathodic scan, the peak current occurs at 0.95 V and 0.63 V for Fe_2O_3@PDA@G due to the reduction of Fe^{3+} or Fe^{2+} to metallic Fe and the irreversible decomposition of the electrolyte to form an SEI film [22]. In addition, the broad peak observed at approximately 1.29 V can be attributed to the insertion of lithium ions into amorphous Fe_2O_3 to form a solid-solution-like compound [15]. The first anodic sweep shows two peaks at approximately 1.59 V and 1.95 V, which indicates the oxidation of metallic Fe to Fe^{2+} and oxidation to Fe^{3+}, respectively. The rate property of the half-cells based on the Fe_2O_3, Fe_2O_3@PDA and Fe_2O_3@PDA@G anodes at different current densities from 100 mAg^{-1} to 5000 mAg^{-1} between 0.01~3 V were also investigated and are shown in Fig. 7. As shown in Fig. 7, with the surface modification of the graphene layer, Fe_2O_3@PDA@G exhibits a higher capacity (100 mAg^{-1}: 887.8 $mAhg^{-1}$; 200 mAg^{-1}: 870.1 $mAhg^{-1}$; 500 mAg^{-1}: 734.9 $mAhg^{-1}$; 1000 mAg^{-1}: 632.9 $mAhg^{-1}$, 2000 mAg^{-1}: 509.3 $mAhg^{-1}$, 5000 mAg^{-1}: 281.5 $mAhg^{-1}$) than Fe_2O_3 (100 mAg^{-1}: 962.7 $mAhg^{-1}$; 200 mAg^{-1}: 562.3 $mAhg^{-1}$; 500 mAg^{-1}: 232.2 $mAhg^{-1}$; 1000 mAg^{-1}: 87.5 $mAhg^{-1}$, 2000 mAg^{-1}: 40.1 $mAhg^{-1}$, 5000 mAg^{-1}: 26 $mAhg^{-1}$) at high current density. Its capacity retention is only approximately 2.7% with respect to the 26 mAg^{-1}discharge specific capacity of the pristine Fe_2O_3 electrode under a 5000 mAg^{-1} current density, while the value can be kept at approximately 32.4% for the Fe_2O_3@PDA@G electrode, as shown in Table. 1. The enhanced rate capability of the Fe_2O_3@PDA@G electrode could be primarily ascribed to the smaller polarization and shorter Li-ion diffusion length of the electrode. These results are consistent with the CV measurements.

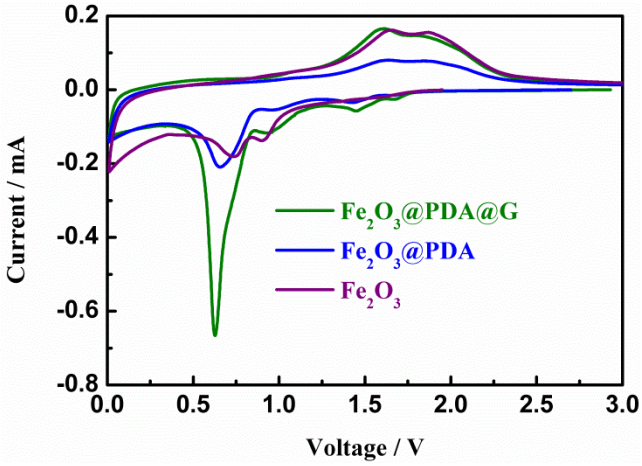

Figure 6. Cyclic voltammetry curves of the Fe_2O_3, Fe_2O_3@PDA and Fe_2O_3@PDA@G electrodes in the first cycle in the voltage range of 0.01~3 V at a scan rate of 0.1 mV/s.

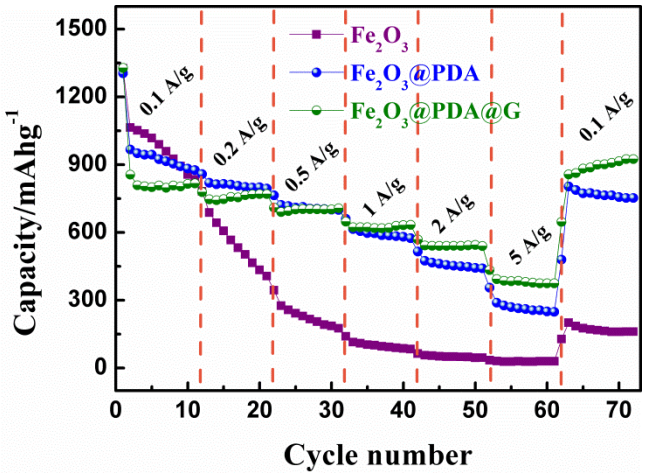

Figure 7. Rate property of the half-cells based on the Fe_2O_3, Fe_2O_3@PDA and Fe_2O_3@PDA@G anodes at different current densities from 100 mAg^{-1} to 5000 mAg^{-1} between 0.01~3 V.

Table 1. Capacity of Fe_2O_3 and Fe_2O_3@PDA@G at different current densities.

	100mAg^{-1}	200mAg^{-1}	500mAg^{-1}	1000mAg^{-1}	2000mAg^{-1}	5000mAg^{-1}
Fe_2O_3 ($mAhg^{-1}$)	962.7	562.3	232.2	87.5	40.1	26
Fe_2O_3@PDA@G ($mAhg^{-1}$)	887.8	870.1	734.9	632.9	509.3	281.5

Fig. 8(a), (b), (c) and (d) show the surface potential maps of the Au, Fe_2O_3, Fe_2O_3@PDA and Fe_2O_3@PDA@G electrodes, respectively, after 90 cycles and were obtained using the KPFM technique to evaluate the electric properties of the materials. In combination with [37], the work functions of Fe_2O_3,

Fe_2O_3@PDA and Fe_2O_3@PDA@G are shown in Fig. 8(e), and results show that the work function of Fe_2O_3@PDA@G (~5.1 eV) is approximately 0.4 eV smaller than that of Fe_2O_3 (~5.6 eV). In this study, the real measured work function of Fe_2O_3 is near the reported value (5.71±0.2 eV)[38]. A smaller work function means that electrons require less energy to escape from the interior of the composite to the surface, thus improving the electrochemical performance of the composite. These results are consistent with the rate performance. The energy-band model can be used to explain the decrease in the work function for Fe_2O_3@PDA@G, which is schematically shown in Fig. 8(f). Based on the difference in work functions between Fe_2O_3@PDA and graphene (4.43 eV)[39], electrons are transferred from graphene with a smaller work function to Fe_2O_3@PDA with a larger work function until the two Fermi levels are aligned. Therefore, 2D graphene networks can improve electrochemical performance, including rate performance and cycle stability.

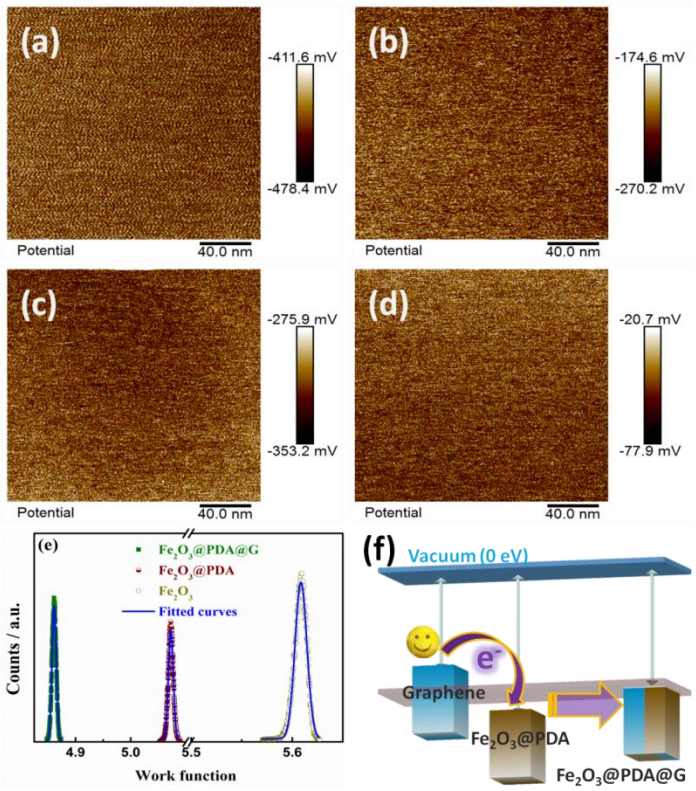

Figure 8. Surface potential maps of the (a)Au, (b) Fe_2O_3, (c) Fe_2O_3@PDA and (d) Fe_2O_3@PDA@G electrodes after 90 cycles; (e) work function distribution curves of Fe_2O_3, Fe_2O_3@PDA and Fe_2O_3@PDA@G; (f) schematic illustration of the energy-band model for graphene, Fe_2O_3@PDA and Fe_2O_3@PDA@G.

4. CONCLUSIONS

In this study, we have fabricated a simple and flexible strategy of graphene sheet-wrapped Fe_2O_3 nanorings by electrostatic incorporation. The hybrid electrode shows excellent cycling stability and superior high-rate capability. The improvement in electrochemical performance can be attributed to the

incorporation of flexible graphene sheets, forming a uniform two-dimensional conductive network that enables electrons to transfer easily and rapidly between the surface of Fe_2O_3 nanorings and graphene sheets, and move unobstructed over the particles to deliver a high rate capability. In addition, the addition of graphene is beneficial to the reversible intercalation/extraction of Li ions. Fe_2O_3@PDA@G has a smaller charge transfer resistance corresponding to a much higher conductivity than Fe_2O_3. The lower work function of Fe_2O_3@PDA@G suggests that electrons require less energy to escape from the interior of the composite to its surface. The results of this study indicate that graphene plays an important role in improving the electrochemical property of the Fe_2O_3 particles, particularly at high current density.

NOTES

The authors declare no competing financial interest.

ACKNOWLEDGMENTS

This study was supported by a grant from the major cultivation program of Ningde Normal University (Grant No. 2019ZDK07, 2019ZX502, 2021ZDK07), the Natural Science Foundations of Fujian Province of China (Grant No. 2020J05258), the Project of Scientific Research of Ningde Normal University (Grant No. 2020Y06, 2020Y017).

References

1. T. L. Kulova, V. N. Fateev, E. A. Seregina and A. S. Grigoriev, Int. J. Electrochem. Sci., 15 (2020) 7242-7259.
2. X. Zhang, Y. Han and W. Zhang, Trans Electr Electro., 22 (2021) 567-574.
3. X. Y. Xiang, D. Liu, X. X. Zhu, K. Fang, K. C. Zhou, H. L. Tang, Z. Z. Xie, J. S. Li, H. Zheng and D. Y. Qu, Appl Surf Sci., 514 (2020) 145947.
4. N. Wu, X. Zhang, C. Ma, Y. R. Shi, J. M. Zhou, Z. Wang, H. Liu, X. X. Zeng and Y. Wei, Electrochimica Acta, 297 (2019) 1028-1034.
5. Y. F. Su, J. J. Zhan, T. Huang, Z. L. Liu and A. S. Yu, *Int. J. Electrochem. Sci.*, 8 (2013) 2918-2931.
6. L. H. Yin, Y. J. Gao, I. Jeon, H. Yang, J. P. Kim, S. Y. Jeong and C. R. Cho, *Chemical Engineering Journal*, 356 (2019) 60-68.
7. J. Q. Jiao, W. D. Qiu, J. G. Tang, L. P. Chen and L. Y. Jing, *Nano Research*, 9 (2016) 1256-1266.
8. Y. T. Zuo, G. Wang, J. Peng, G. Li, Y. Q. Ma, F. Yu, B. Dai, X. H. Guo and C. P. Wong, *J. Mater. Chem. A*, 4 (2016) 2453-2460.
9. Y. J. Wang, S. B. Huang, Y. Lu, S. Z. Cui, W. H. Chen and L. W. Mi, *RSC Adv.*, 7 (2017) 3752-3759.
10. F. Zhang, C. K. Yang, X. Gao, S. Chen, Y. R. Hu , H. Q. Guan, Y. R. Ma, J. Zhang, H. H. Zhou and L. M. Qi, *ACS Appl. Mater. Interfaces*, 9 (2017) 9620-9629.
11. F. Y. Zeng, Y. F. Ren, L. Chen, Y. Yang, Q. L. Li and G. Gu, *Electrochimica Acta*, 190 (2016) 964-971.
12. S. Q. Zhao, T. M. Liu, D. W. Hou, W. Zeng, B. Miao, S. Hussain and X. H. Peng, *Applied Surface Science*, 356 (2016) 259-265.
13. J. L. Yang, Q. L. Wu, X. F. Yang, S. M. He, J. Khan, Y. Y. Meng, X. M. Zhu, S. F. Tong and M. M. Wu, *ACS Appl. Mater. Interfaces*, 9 (2017) 354-361.
14. Y. Q. Fu, Q. L. Wei, B. Lu, X. Y. Wang and S. H. Sun, *Journal of Alloys and Compounds*, 684 (2016) 419-427.
15. Y. Huang, Z. X. Lin, M. B. Zheng, T. H. Wang, J. Z. Yang, F. S. Yuan, X. Y. Lu, L. Liu and D. P.

Sun, *Journal of Power Sources*, 307 (2016) 649-656.
16. Q. S. Zhao, J. L. Liu, X. X. Li, Z. Z. Xia, Q. X. Zhang, M. Zhou, W. Tian, M. Wang, H. Hu, Z. T. Li, W. T. Wu, H. Ning and M. B. Wu, *Chemical Engineering Journal*, 369 (2019) 215-222.
17. G. D. Zhang, Y. H. Shi, H. R. Wang, L. L. Jiang, X. D. Yu, S. Y. Jing, S. X. Xing and P. Tsiakaras, *Journal of Power Sources*, 416 (2019) 118-124.
18. Y. Wang, J. Roller and R. Marica, *Journal of Power Sources*, 2018, 378, 511-515.
19. Y. Wang, P. D. Mao, F. F. Yan, C. W. Gao, Y. H. Liu, J. Ding, W. N. Wu and Y. S. Liu, *Synthetic Metals*, 222 (2016) 198-204.
20. J. S. Cho, Y. J. Hong and Y. C. Kang, *ACS Nano*, 9 (2015) 4026-4035.
21. Z. Y. Wang, D. Y. Luan, S. Madhavi, Y. Hu and X. W. (David) Lou, *Energy Environ. Sci.*, 5 (2012) 5252-5256.
22. W. S. Xiong, Y. Jiang, Y. Xia, Y. Y. Qi, W. W. Sun, C. L. Hu, R. X. He, B. Chen, Y. M. Liu and X. Z. Zhao, *Journal of Power Sources*, 401 (2018) 65-72.
23. C. J. Fu, C. L. Song, L. L. Liu, X. D. Xie and W. L. Zhao, *Int. J. Electrochem. Sci.*, 11 (2016) 3876-3886.
24. S. Z. Huang, Y. Li, Y. Y. Feng, H. R. An, P. Long, C. Q. Qin and W. Feng, *J. Mater. Chem. A*, 3 (2015) 23095-23105.
25. Y. Chen, J. Zhu, B. Qu, B. Lu and Z. Xu, *Nano Energy*, 3 (2014) 88-94.
26. Y. Gu, Z. Jiao, M. H. Wu, B. Luo, Y. Lei, Y. Wang, L. Z. Wang and H. J. Zhang, *Nano Research*, 10 (2017) 121-133.
27. H. Y. Yang, X. H. Yu, H. W. Meng, P. Dou, D. Q. Ma and X. H. Xu, *J Mater Sci.*, 50 (2015) 5504-5513.
28. Q. Qu, J. Chen, X. Li, T. Gao, J. Shao and H. Zheng, *J. Mater. Chem. A,* 3 (2015) 18289-18295.
29. K. Lee, S. Shin, T. Degenc, W. Lee and Y. S. Yoon, *Nano Energy*, 32 (2017) 397-407.
30. Z. Y Lin, G. Z. Liu, Y. P. Zheng, Y. B. Lin and Z. G. Huang, *J. Mater. Chem. A*, 6 (2018) 22655-22661.
31. X. X. Li, X. Y. Zheng, J. Shao, T. Gao, Q. Shi and Q. T. Qu, *Chem. Eur. J.*, 22 (2016) 376-381.
32. Y. Z. Yan, H. L. Tang, J. S. Li, F. Wu, T. B. Wu, R. Wang, D. Liu, M. Pan, Z. Z. Xie and D. Y. Qu, *Journal of Colloid and Interface Science*, 495 (2017) 157-167.
33. C. C. Chen, Y. N. Huang, H. Zhang, X. F. Wang, G. Y. Li, Y. J. Wang, L. F. Jiao and H. T. Yuan, *Journal of Power Sources*, 278 (2015) 693-702.
34. M. Z. Zou, J. X. Li, W. W. Wen, L. Z. Chen, L. H. Guan, H. Lai and Z. G. Huang, *Journal of Power Sources*, 270 (2014) 468-474.
35. W. T. Song, J. Xie, S. Y. Liu, G. S. Cao, T. J. Zhu and X. B. Zhao, *New J. Chem.*, 36 (2012) 2236-2241.
36. M. Du, J. Sun, J. Chang, F. Yang, L. J Shi and Lian Gao, *RSC Adv.*, 4 (2014) 42412-42417.
37. L. C. Chen, Y. M. Yang, Z. S. Wang, Z. Y. Lin, J. Y. Zhang, Q. L., Y. Chen, W. Chen, Y. B. Lin and Z. G. Huang, *Journal of Alloys and Compounds*, 711 (2017) 462-472.
38. W. Zhang and Y. S. Chen, *J Nanopart Res.*, 15 (2013) 1334-1340.
39. X. W. Wang, G. Z. Sun, P. Routh, D. -H. Kim, W. Huang and P. Chen, *Chem. Soc. Rev.*, 43 (2014) 7067-7098.